Colloid Polym Sci (2012) 290:385–400
DOI 10.1007/s00396-011-2564-z

ORIGINAL CONTRIBUTION

Aggregation behavior of thermo-responsive poly(2-oxazoline)s at the cloud point investigated by FCS and SANS

Stephan Salzinger · Stephan Huber · Sebastian Jaksch · Peter Busch · Rainer Jordan · Christine M. Papadakis

Received: 25 August 2011 / Revised: 15 November 2011 / Accepted: 1 December 2011 / Published online: 27 December 2011

Abstract We have studied different thermo-responsive poly(2-oxazoline)s with *iso*-propyl (*i*PrOx) and *n*-propyl (*n*PrOx) pendant groups in aqueous solutions, where they exhibit lower critical solution temperature behavior. This paper focuses on the effect of the degree of polymerization, *n*, the concentration, *c*, in the dilute regime, and the presence of hydrophobic moieties. The cloud points were investigated as a function of the degree of polymerization, *n*, and of the polymer concentration, *c*. The aggregation behavior near the cloud point was studied by temperature-resolved small-angle neutron scattering and fluorescence correlation spectroscopy, i.e., a combination of ensemble and single molecule methods. We found that at the cloud points, large aggregates are formed and that the cloud points depend strongly on both, *n* and *c*. Diblock copolymers from *i*PrOx and *n*PrOx form large aggregates already at the cloud point of P*n*PrOx, and, unexpectedly, no micelles are observed between the cloud points of the two blocks. Gradient copolymers from *i*PrOx and *n*-nonyl-2-oxazoline (NOx) display a complex aggregation behavior resulting from the interplay between intra- and intermolecular association mediated by the hydrophobic NOx blocks. Above the cloud point, an intermediate temperature regime with a width of a few Kelvin was found with small but stable polymer aggregates. Only at higher temperatures, larger aggregates are found in significant number.

Keywords Polyoxazoline · Cloud point · Thermo-responsive polymers · Small-angle neutron scattering · Fluorescence correlation spectroscopy

Stephan Salzinger, Stephan Huber and Sebastian Jaksch equally contributed to this paper.

S. Salzinger · S. Huber · R. Jordan
Technische Universität München, Department Chemie,
WACKER-Lehrstuhl für Makromolekulare Chemie,
Lichtenbergstr. 4,
85747 Garching, Germany

S. Jaksch · C. M. Papadakis (✉)
Technische Universität München, Physikdepartment,
Fachgebiet Physik weicher Materie,
James-Franck-Str. 1,
85747 Garching, Germany
e-mail: Papadakis@tum.de

S. Jaksch
e-mail: sebastian.jaksch@tum.de

P. Busch
Forschungszentrum Jülich GmbH,
Jülich Centre for Neutron Science at FRM II,
Lichtenbergstr. 1,
85747 Garching, Germany

R. Jordan (✉)
Department Chemie, Professur für Makromolekulare Chemie,
Technische Universität Dresden,
Zellescher Weg 19,
01069 Dresden, Germany
e-mail: Rainer.Jordan@tu-dresden.de

Introduction

Thermo-responsive polymers have received increasing attention as they respond in a defined and reversible way by a volume change to small changes of temperature and are therefore of great interest as smart materials for biomedical applications [1–3] and in materials science, e.g., for porous membranes for molecular filtration where the permeability can be controlled by a change of temperature across the cloud point of the polymer [4–6]. However, the polymer chain collapse at the cloud point is still not completely understood. Most investigations of thermo-responsive polymers focus on poly(*N*-isopropylacrylamide) (PNIPAM). Its lower critical solution temperature (LCST) at ~32 °C is attributed to alterations in the hydrogen-bonding interactions of amide group

acting as the H-donor and H-acceptors [7–9]. The cloud point of water-soluble polymers depends on a number of parameters, such as the average molar mass and concentration, which has been attributed to sequential hydrogen bond formation between PNIPAM and water [10]. Although the cloud point of PNIPAM and numerous other polymers was intensively investigated, detailed studies of the aggregation with structurally defined polymer systems are rare, and it is desirable to better understand the mechanisms leading to the polymer collapse at the cloud point on the molecular level. In contrast to PNIPAM, thermo-responsive POx have a very sharp solubility transition, typically within ±1 °C, with the cloud point showing only a minor or no transition hysteresis for sufficiently high polymer concentration. This is explained by the fact that POx (similar to poly(ethylene glycol) (PEG) can only act as an acceptor in hydrogen bonding, whereas PNIPAM can act both as an acceptor and a donor.

Moreover, POx are especially interesting because the hydrophilicity of each monomer unit can be fine-tuned by the pendant 2-substitution. While poly(2-methyl-2-oxazoline) is highly hydrophilic, poly(2-ethyl-2-oxazoline) is water soluble, but already shows a slight amphiphilicity [11], whereas longer alkyl side groups result in increasing amphiphilicity and the POx with 2-*n*- or 2-*iso*-alkyl chains with 2–3 hydrocarbon units show a defined cloud point in a similar range as PNIPAM. With a further increase of the hydrocarbon side chain length, POx becomes a polysoap with a strong amphiphilic contrast in each monomer unit. The carbon number of the pendant group can be used to modulate the LCST of the homopolymer within a broad temperature range. For copolymers (random or gradient) the introduction of hydrophilic 2-oxazoline monomer units increases the LCST, whereas hydrophobic ones decrease the LCST [12–15]. The same strategy can be used to tune the LCST by the polarity of the polymer end-groups [12]. Recently, Luxenhofer et al. [16] used this subtle tailoring of the hydrophilic/hydrophobic balance of POx to realize doubly amphiphilic block copolymers with a moderately hydrophobic core and hydrophilic tails for a drug-delivery system with extremely high loading capacities of hydrophobic drugs such as paclitaxel. The POx system furthermore allows for the introduction of additional chemical functionalizations in the polymer side chains as well as at the chain termini, such as carboxylic acid [17], amine [18], aldehyde [19],thiol [20], alkene [21], and alkine [22] groups, to name a few. Together with the possibility of structural tuning, novel amphiphilic block copolymers for micellar catalysis could be realized [23] which served as nanoreactors for atom transfer radical polymerization [24], metathesis [25], and the asymmetric hydrogenation of amino acid precursors [26, 27]. Especially the possibilities of the site-selective introduction of fluorescence labels are of great importance for correlating the observed physical properties of the supramolecular aggregates with the specific polymer architecture, e.g. with fluorescence correlation spectroscopy (FCS) [28–30]. For biomedical applications the POx system is especially interesting as hydrophilic POx are nontoxic [31–35] and display an advantageous biodistribution and excretion behavior [36]. Thus, POx are currently under intense study for biological and biomedical applications [37–39] such as drug-delivery, biohybrid [40, 41], and biomimetic [42–52] systems such as artificial cell membranes.

These possibilities for functionalization greatly promote the range of applications of POx systems, especially when combined with their thermo-responsive properties. The LCST of POx was first reported on poly(2-ethyl-2-oxazoline)s by Lin et al. [53]. Later on, more detailed reports on the same polymer completed this picture [54], and very soon on, the synthetic possibilities of the variation of the polymer composition and combination of 2-oxazoline monomers having different pendant 2-alkyl-chains were used to precisely modulate the LCST of POx in a wide range [12–15, 55–57]. Moreover, the effect of the POx end-group was studied [12, 58, 59], and the LCST behavior of novel POx-based molecular brushes [60–63] and graft copolymers [64] was investigated. The LCST behavior and aggregation of poly(2-*iso*-propyl-2-oxazoline) (P*i*PrOx) was found to be unusual because it exhibits an irreversible crystallization at prolonged heating above the LCST [65].

We have previously investigated the aggregation behavior of POx in water as a function of their composition, architecture and hydrophilic–lipophilic balance (HLB). Diblock copolymers from 2-methyl-2-oxazoline (MOx) and 2-*n*-nonyl-2-oxazoline (NOx) were found to have very low critical micelle concentrations in aqueous solution, typical for nonionic polysoaps [28, 30]. Triblock and gradient copolymers also formed micelles of sizes that are defined by the polymer chain architecture [29]. These investigations were carried out using FCS on P(MOx-*b*-NOx) labeled with tetramethylrhodamineisothiocyanate (TRITC) at either terminus. Small-angle neutron scattering (SANS) allowed us to investigate the micellar size, structure and shape in detail and to verify the core-shell structure for diblock copolymers from MOx, NOx as well as perfluorinated 2-oxazolines [66].

For the investigation of the aggregation behavior of thermo-responsive polymers, classical macroscopic methods such as turbidimetry are often combined with scattering experiments such as static and dynamic light scattering or small-angle X-ray or neutron scattering (SAXS and SANS). These methods, however, suffer from poor statistics if the polymer concentration is very low. FCS can provide more details on the aggregation behavior especially at very low concentrations, e.g., below the CMC where only individually solubilized macromolecules (unimers) are of interest.

A number of FCS studies of synthetic macromolecular systems have been reported: Fluorescence homopolymers in solution [67, 68] and at the air–water interface were studied [69–72]. Polymer gels were investigated both in the bulk and anchored to solid substrates [73, 74], as well as protein diffusion through polymer gels [75]. The micellization of diblock copolymers was investigated by adding a poorly water-soluble fluorescence agent to the solution [76–78]. Its solubility in the micellar core enabled the detection of the micelles, the determination of their hydrodynamic radius and to detect the CMC [76], which, in polymers, usually is very low. In a study on so-called Janus micelles, the CMC in selective solvent could be determined using FCS [79]. The reliability of FCS to characterize micellar solutions from amphiphilic block copolymers with fluorescent dyes was proven as well [80]. In bulk polymers, both melts and blends were investigated [81], also with focus on the chain end topology of the polymers [82]. Bulk polymers in thin film geometry were investigated with respect to the segmental dynamics [83] and to the effect of polymer viscosity on the rotational diffusion of the fluorescent dye [84].

In the present work, we investigate the aggregation behavior of thermo-responsive POx with 2-*iso*-propyl pendant groups (P*i*PrOx) in aqueous solution. Their cloud points are determined using turbidimetry and are found to depend strongly on concentration in the range c=0.5–20 mg/mL. A set of identical polymers from the same batch were additionally fluorescence-labeled with TRITC for temperature-resolved FCS. By this way, we have characterized the aggregation behavior as a function of the average degree of polymerization, n, in dilute solution in the range n=25–50. To investigate the role of the polymer pendant group, poly(2-*n*-propyl-2-oxazoline) (P*n*PrOx) homopolymers of the same degree of polymerization, n, were prepared and investigated in a second set of FCS experiments. Beside the P*i*PrOx and P*n*PrOx homopolymers, diblock copolymers from *i*PrOx and *n*PrOx were investigated and were found to form large aggregates already at the lowest cloud point (the one of P*n*PrOx). Moreover, gradient copolymers with few hydrophobic NOx monomers in a thermo-responsive P*i*PrOx chain were synthesized. This allowed us to study the influence of a few but strongly hydrophobic moieties along the polymer chain on the aggregation behavior. Thus, by varying n and c, and by inserting different side groups and additional alkyl moieties as hydrophobic domains, the cloud point can be tuned in a large range, and the aggregation process can be modified.

These investigations add to previous work on poly(2-ethyl-2-oxazoline) [53, 54] and on P*i*PrOx where the focus was on the end-group polarity [12] and on gradient copolymers from *i*PrOx with various hydrophobic comonomers [56].

Experimental

Materials for synthesis

All chemicals used for synthesis were purchased from Sigma-Aldrich (Steinheim, Germany), Acros Organics (Geel, Belgium), or Fluka (Steinheim, Germany) and were used without further purification unless otherwise stated. Deuterated solvents for NMR spectroscopy were purchased from Deutero GmbH (Kastellaun, Germany). NOx was received as a gift from Henkel KGaA (Düsseldorf, Germany).

Solvents, methyltriflate (MeOTf) and all monomers used for the living cationic polymerization were dried by refluxing over CaH_2 for approximately 3 h and subsequent distillation. The chemicals were stored under dry nitrogen atmosphere and handled in a glove box under dry argon. As terminating agent, a solution of piperazine in dry chloroform (0.375 g/mL) was prepared and stored under dry nitrogen.

Characterization methods

Spectroscopy

^{1}H- and ^{13}C-NMR spectra were recorded on a Bruker ARX 300 (^{1}H, 300.13 MHz and ^{13}C, 75.47 MHz) in $CDCl_3$. The residual solvent signal of $CHCl_3$ was used as internal standard (δ=7.26 ppm for ^{1}H-NMR and δ=77.0 ppm for ^{13}C-NMR; ppm relative to tetramethylsilane). FTIR spectroscopy was carried out using a Bruker IFS 55s spectrometer equipped with an ATR set-up from Harrick (single bounce, diamond crystal) and an MCT detector.

Gel permeation chromatography

Gel permeation chromatography (GPC) was performed on a Waters system (pump mod. 510 and RI-detector mod. 410) with columns Resi Pore Guard (50×7.5 mm) and 2× Resi Pore (300×7.5 mm) as the stationary and dimethyl acetamide as the mobile phase. The calculation of the molar mass and number average (M_w and M_n) was performed using a calibration with polystyrene standards.

Elemental analysis

Elemental analysis was performed using an Elementar-Vario EL instrument at the Microanalytical Laboratory of the Inorganic Chemistry Institute of the TU München.

Synthesis

Monomer synthesis

2-*iso*-propyl-2-oxazoline (*i*PrOx) and 2-*n*-propyl-2-oxazoline (*n*PrOx) were synthesized according to Seeliger et al. [85]. A 100-mL round bottomed flask was charged with a catalytical amount of cadmium acetate dihydrate, 1.2 eq of aminoethanol and 1 eq of isobutyro- or *n*-butyronitrile, respectively. The reaction mixture was heated to 125 °C and stirred for 16 h. The red raw product was purified by vacuum distillation, the obtained 2-oxazoline dried over CaH_2 and then stored under dry nitrogen for later use.

2-iso-propyl-2-oxazoline, iPrOx Yield: 17.4 g (71%). bp: 56 °C at 65 mbar. ^{1}H-NMR: (292 K, $CDCl_3$): δ (ppm)=1.18 (d, 6H, ^3J=7.0 Hz, –CH_3), 2.53 (m, 1H, –CH–(CH_3)$_2$), 3.80 (t, 2H, ^3J=9.5 Hz, CH_2–CH_2–N), 4.21 (t, 2H, ^3J=9.5 Hz, O-CH_2-CH_2). ^{13}C-NMR: (300 K, $CDCl_3$): δ (ppm)=19.60 (s, 2C, –*C*H_3), 28.00 (s, 1C, –CH–(–CH_3)$_2$), 54.20 (s, 1C,CH_2–CH_2–N), 67.13 (s, 1C,O–CH_2–CH_2), 172.55 (s, 1C, O-*C*=N). Elemental analysis: found in percent (calculated in percent) C: 63.21 (63.68), H: 10.26 (9.80), N: 12.50 (12.38).

2-n-propyl-2-oxazoline, nPrOx Yield: 10.0 g (50%). bp: 68 °C at 40 mbar. ^{1}H-NMR: (300 K, $CDCl_3$): δ (ppm)= 0.87 (t, 3H, ^3J=7.4, Hz, –CH_3), 1.56 (sextett, 2H, ^3J=7.4, CH_2-CH_2–CH_3), 2.15 (m, 2H, C–CH_2-CH_2), 3.73 (t, 2H, ^3J=9.4 Hz, CH_2–CH_2–N), 4.12 (t, 2H, ^3J=9.4 Hz, O–CH_2–CH_2). ^{13}C-NMR:(300 K, $CDCl_3$): δ (ppm)=13.56 (s, 1C, –*C*H_3), 19.20 (s, 1C, CH_2-*C*H_2–CH_3), 29.67 (s, 1C, *C*H_2-CH_2–CH_3), 54.19 (s, 1C,CH_2–CH_2–N), 66.89 (s, 1C,O–CH_2–CH_2), 168.23 (s, 1C, O-C=N). Elemental analysis: found in percent (calculated in percent) C: 62.95 (63.68), H: 10.27 (9.80), N: 13.01 (12.38).

Polymerization

All polymerizations were carried out using a CEM Discover microwave with a maximum power setting of 150 W. The microwave was set to a reaction temperature of 130 °C that was continuously monitored by an internal infrared detector.

In a typical polymerization reaction, a microwave vial was charged with methyl triflate in dry acetonitrile. The monomer was added to the reaction mixture (both in case of gradient copolymers), and the polymerization was carried out in the microwave reactor at 130 °C for 30 min for n=25, 50 min for n=50 and two times 30 min for the block copolymers. Afterwards, piperazine (0.375 g/mL in $CHCl_3$) was injected into the reaction mixture at room temperature; 20 eq of terminating agent were used in order to prevent double termination. The solution was stirred overnight at room temperature. Finally, the solvent as well as the excess of the terminating agent was removed under vacuum and the residue was dissolved in chloroform and stirred with dry potassium carbonate for at least 4 h at room temperature. After filtration, the polymer was purified by precipitation ($CHCl_3$ to ether), dialysis in water and freeze drying (water). All polymers were received as colorless powders.

Poly(2-iso-propyl-2-oxazoline)$_{25}$ Yield: 0.92 g (75%). ^{1}H-NMR: (292 K, $CDCl_3$): δ (ppm)=1.09 (br, 150H, side chain-CH_3), 2.30–3.00 (br, 33H, CH_2^{Pip}, -C*H*-(CH_3)$_2$), 3.06 (s, 3H, initiator–CH_3), 3.44 (br, 100H, –N–CH_2–CH_2–N–). M_n (^{1}H-NMR end-group analysis): 2,929 g/mol. IR: in cm^{-1}: (CH_3): 2,967, (CH_2): 2,934, (CH): 2,873, (amide-CO): 1,629, 1,473, 1,424, 1,381, 1,363, 1,308, 1,236, 1,201, 1,157, 1,087, 930, 753. Đ=1.24 (from GPC).

Poly(2-n-propyl-2-oxazoline)$_{25}$; PnPrOx$_{25}$ Yield: 0.96 g (78%). ^{1}H-NMR: (292 K, $CDCl_3$): δ (ppm)=0.93 (br, 75H, side chain-CH_3), 1.62 (br, 50H, CH_2-CH_2–CH_3), 2.00–2.40 (br, 50H, CH_2-CH_2–CH_3), 2.47 (br, 4H, (CH_2^{Pip})$_2$-NH), 2.69 (br, 4H, (CH_2^{Pip})$_2$-*N*-polymer), 3.02 (s, 3H, initiator-CH_3), 3.44 (br, 100H, –N–CH_2–CH_2–N–). M_n (^{1}H-NMR end-group analysis): 2,929 g/mol. IR: in cm^{-1}: (CH_3): 2,962, (CH): 2,875, (amide-CO): 1,638, 1,457, 1,422, 1,377, 1,194, 1,073, 904, and 754. Đ=1.30 (from GPC).

Poly(2-iso-propyl-2-oxazoline)$_{40}$ Yield: 1.27 g (86%). ^{1}H-NMR: (300 K, $CDCl_3$): δ (ppm)=1.09 (br, 240H, side chain-CH_3), 2.45–3.00 (br, 48H, CH_2^{Pip}, -CH-(CH_3)$_2$), 3.03 (s, 3H, initiator-CH_3), 3.44 (br, 160H, –N–CH_2–CH_2–N–). M_n (^{1}H-NMR-end group analysis): 4,626 g/mol. IR: in cm^{-1}: (CH_3): 2,967, (CH_2): 2,934, (CH): 2,873, (amide-CO): 1,630, 1,473, 1,425, 1,381, 1,363, 1,236, 1,202, 1,158, 1,087, 930, and 753. Đ=1.19 (from GPC).

Poly(2-iso-propyl-2-oxazoline)$_{50}$; PiPrOx$_{50}$ Yield: 1.15 g (78%). ^{1}H-NMR: (300 K, $CDCl_3$): δ (ppm)=1.09 (br, 300H, side chain-CH_3), 2.45–3.00 (br, 58H, CH_2^{Pip}, -CH-(CH_3)$_2$), 3.06 (s, 3H, initiator-CH_3), 3.44 (br, 200H, –N–CH_2–CH_2–N–). M_n (^{1}H-NMR end-group analysis): 5,758 g/mol. IR: in cm^{-1}: (CH_3): 2,967, (CH_2): 2,933, (CH): 2,872, (amide-CO): 1,633, 1,423, 1,361, 1,201, 1,157, 1,086, and 928. Đ=1.17 (from GPC).

Poly(2-n-propyl-2-oxazoline)$_{50}$ Yield: 1.24 g (86%). ^{1}H-NMR: (292 K, $CDCl_3$): δ (ppm)=0.93 (br, 150H, side chain-CH_3), 1.61 (br, 100H, CH_2-CH_2–CH_3), 2.00–2.40 (br, 100H, CH_2-CH_2–CH_3), 2.45–2.75 (br, 8H, (CH_2^{Pip})$_2$–NH, (CH_2^{Pip})$_2$-*N*-polymer), 3.43 (br, 200H, –N–CH_2–CH_2–N–). M_n (^{1}H–NMR end-group analysis): 5,758 g/mol. IR: in cm^{-1}: (CH_3): 2,961, (CH): 2,873, (amide-CO): 1,620, 1,418, 1,375, 1,190, 1,071, 901, and 753. Đ=1.40 (from GPC).

Poly[(2-n-propyl-2-oxazoline)$_{25}$-block-(2-iso-propyl-2-oxazoline)$_{25}$] Yield: 2.48 g (86%). ^{1}H-NMR: (292 K, $CDCl_3$): δ (ppm)=0.92 (br, 75H, *n*-propyl-CH_3), 1.08 (br, 150H, *iso*-propyl-CH_3), 1.62 (br, 50H, CH_2-CH_2–CH_3), 2.00–2.40 (br, 50H, CH_2-CH_2–CH_3), 2.45–2.95 (br, 33H, CH_2^{Pip}, -CH-$(CH_3)_2$), 3.03 (s, 3H, initiator-CH_3), 3.43 (br, 200H, –N–CH_2–CH_2–N–). M_n (^{1}H-NMR end-group analysis): 5,758 g/mol. Monomer ratio (^{1}H-NMR): 25:25. IR: in cm^{-1}: (CH_3): 2,965, (CH): 2,875, (amide-CO): 1,629, 1,473, 1,422, 1,361, 1,221, 1,198, 1,159, 1,088, and 904. $Đ$=1.36 (from GPC).

Poly[(2-iso-propyl-2-oxazoline)$_{48}$-(2-n-nonyl-2-oxazoline)$_2$]$_{grad}$ Yield: 1.14 g (77%). ^{1}H-NMR: (292 K, $CDCl_3$): δ (ppm)=0.86 (br, 6H, *n*-nonyl-CH_3), 1.09 (br, 288H, *iso*-propyl-CH_3), 1.24 (br, 24H, CH_2–$(CH_2)_6$–CH_3), 1.57 (br, 4H, CH_2-CH_2–$(CH_2)_6$–CH_3), 2.31 (br, 4H, CH_2-CH_2–$(CH_2)_6$–CH_3), 2.45–3.00 (br, 56H, CH_2^{Pip}, -CH-$(CH_3)_2$), 3.06 (s, 3H, initiator-CH_3), 3.44 (br, 200H, –N–CH_2–CH_2–N–). M_n (^{1}H-NMR end-group analysis): 5,926 g/mol. Monomer ratio (^{1}H-NMR): 48:2. IR: in cm^{-1}: (CH_3): 2,966, (CH_2): 2,933, (CH): 2,872, (amide-CO): 1,630, 1,473, 1,423, 1,381, 1,361, 1,221, 1,201, 1,157, 1,086, 1,033, 929, and 753. $Đ$=1.19 (from GPC).

Poly[(2-iso-propyl-2-oxazoline)$_{46}$-(2-n-nonyl-2-oxazoline)$_4$]$_{grad}$ Yield: 1.21 g (80%). ^{1}H-NMR: (292 K, $CDCl_3$): δ (ppm)=0.86 (br, 12H, *n*-nonyl-CH_3), 1.09 (br, 288H, *iso*-propyl-C*H*$_3$), 1.24 (br, 48H, CH_2–(C*H*$_2$)$_6$–CH_3), 1.58 (br, 8H, CH_2-CH_2–$(CH_2)_6$–CH_3), 2.31 (br, 8H, CH_2-CH_2–$(CH_2)_6$–CH_3), 2.45–3.00 (br, 54H, CH_2^{Pip}, -CH-$(CH_3)_2$), 3.06 (s, 3H, initiator-CH_3), 3.44 (br, 200H, –N–CH_2–CH_2–N–). M_n (^{1}H-NMR end-group analysis): 6,094 g/mol. Monomer ratio (^{1}H-NMR): 46:4. IR: in cm^{-1}: (CH_3): 2,965, (CH_2): 2,931, (CH): 2,872, (amide-CO): 1,632, 1,473, 1,422, 1,380, 1,362, 1,200, 1,157, 1,086, 929, and 753. $Đ$=1.19 (from GPC).

Fluorescence labeling

Fluorescence labeling was performed according to a procedure described before [28]. Analysis of the product by GPC and FTIR spectroscopy revealed that the labeling was not quantitative and that the product does not contain free dye. However, as, for the FCS studies, only very small amounts of labeled polymers are to be added and mixtures of labeled and unlabeled POx are used, the incomplete labeling does not affect the results of the FCS experiments. The FTIR analysis and labeling efficiency are as follows: P*i*PrOx$_{25}$-TRITC: yield: 40 mg (69%). IR: in cm^{-1}: (CH_3): 2,966, (CH_2): 2,933, (CH): 2,872, (amide-CO): 1,634, 1,472, 1,422, 1,381, 1,362, 1,305, 1,233, 1,199, 1,156, 1,086, 930, and 753. P*n*PrOx$_{25}$-TRITC: Yield: 34 mg (59%). IR: in cm^{-1}: (CH_3): 2,961, (CH): 2,874, (amide-CO): 1,635, 1,419, 1,377, 1,318, 1,191, 1,157, 1,098, 1,072, 903, and 754. Poly(2-*iso*-propyl-2-oxazoline)$_{40}$ (P*i*PrOx$_{40}$)-TRITC: Yield: 48 mg (88%). IR: in cm^{-1}: (CH_3): 2,966, (CH_2): 2,933, (CH): 2,872, (amide-CO): 1,634, 1,471, 1,421, 1,380, 1,362, 1,305, 1,233, 1,199, 1,156, 1,086, 1,038, 930, and 752. P*i*PrOx$_{50}$-TRITC: Yield: 43 mg (80%). IR: in cm^{-1}: (CH_3): 2,967, (CH_2): 2,934, (CH): 2,873, (amide-CO): 1,641, 1,475, 1,427, 1,200, 1,159, 1,088, and 752. Poly(2-*n*-propyl-2-oxazoline)$_{50}$ (P*n*PrOx$_{50}$)-TRITC: Yield: 44 mg (81%). IR: in cm^{-1}: (CH_3): 2,961, (CH): 2,874, (amide-CO): 1,632, 1,418, 1,376, 1,238, 1,189, 1,098, 1,072, 903, and 754. P(*n*PrOx$_{25}$-*b*-*i*PrOx$_{25}$)-TRITC: Yield: 39 mg (73%). IR: in cm^{-1}: (CH_3): 2,964, (CH_2): 2,933, (CH): 2,873, (amide-CO): 1,620, 1,472, 1,423, 1,364, 1,237, 1,197, 1,160, 1,088, 928, and 754. P(*i*PrOx$_{48}$NOx$_2$)$_{grad}$-TRITC: Yield: 51 mg (93%). IR: in cm^{-1}: (CH_3): 2,966, (CH_2): 2,932, (CH): 2,872, (amide-CO): 1,633, 1,471, 1,421, 1,378, 1,306, 1,234, 1,198, 1,156, 1,086, 933, and 753. P(*i*PrOx$_{46}$-NOx$_4$)$_{grad}$-TRITC: Yield: 50 mg (91%). IR: in cm^{-1}: (CH_3): 2,965, (CH_2): 2,931, (CH): 2,872, (amide-CO): 1,634, 1,471, 1,421, 1,381, 1,362, 1,234, 1,199, 1,156, 1,086, 930, and 753.

TRITC IR: in cm^{-1}: 1,706, 1,646, 1,592, 1,484, 1,405, 1,343, 1,185, 1,131, and 925.

Methods for characterization of the aggregation behavior

Turbidimetry

A Cary 3 UV–vis spectrometer from Varian was operated to measure the transmittance at λ=550 nm. Solutions of the nonlabeled polymers at c=0.5–20 mg/mL in H_2O were heated at a rate of 1 Kmin^{-1} in steps of 1 K, followed by a 3-min equilibration time. The transmittance of the solutions was set to 100% at the beginning of each measurement. The cloud point was defined at the respective temperature with 90% transmittance. Because the transition is very sharp, the accuracy of this procedure is not worse than 1 K.

Fluorescence correlation spectroscopy

A ConfoCor2 spectrometer (Carl Zeiss Jena GmbH) was used as previously described in Ref. [28]. As a light source, a HeNe-Laser with an emission wavelength of 543 nm was used. The measurements were carried out with a pinhole diameter of 70–78 μm and a 2-s bleaching time before the measurement. A Zeiss Plan-Neofluar 40×/1.3 oil objective in combination with the immersion

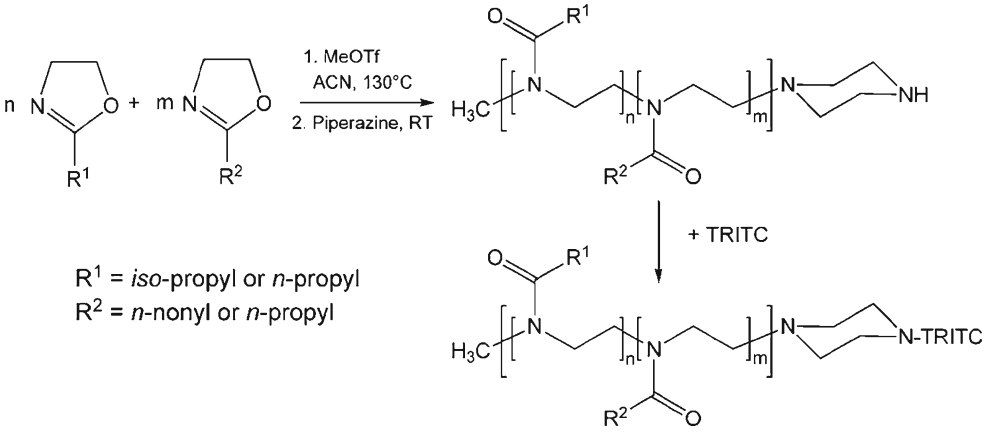

Scheme 1 Living cationic ring-opening polymerization of 2-oxazolines to the homo-, block, and gradient copolymers as well as the polymer analogue coupling of the fluorescence label tetramethylrhodamineisothiocyanate (*TRITC*) via the free secondary amine group of the piperazine at the polymer terminus

oil Zeiss Immersol™ 518F was used for measurements at elevated temperatures. At each temperature, ten measurements of 100-s duration were carried out. The autocorrelation curves were analyzed using the Zeiss LSM 510 ConfoCor 2 software version 3.2 SP2 following Ref. [86]:

$$G(\tau) = 1 + \frac{1}{N} \times \sum_{i=1}^{k} \frac{\rho_i}{\left(1 + \frac{\tau}{\tau_{D,i}}\right)\sqrt{1 + \frac{1}{S^2} \cdot \frac{\tau}{\tau_{D,i}}}} \times \left[1 + \frac{T_T}{1 - T_T} \times \exp\left(-\frac{\tau}{\tau_T}\right)\right] \quad (1)$$

where N is the average total number of fluorescent particles in the detection volume, k the number of different fluorescent species, τ the decay time, $\tau_{D,i}$ the characteristic diffusion time of component i, ρ_i the relative amplitude of the fluorescent species (i.e., the fraction of component i), $S=z_0/w_0$ the axial ratio of the detection volume with radii of the detection volume in beam direction z_0 and normal to beam direction w_0. τ_T is the triplet time and T_T the triplet fraction. In the fit, S was fixed at 1,000, τ_T at 10 μs, and T_T was typically between 5% and 20%.

To determine the diffusion coefficient of the unimers or aggregates, a calibration with a fluorophore with a known diffusion coefficient was carried out. We therefore used Rhodamine 6G ($D_{Rh6G}=2.8\cdot10^{-10}\cdot m^2 s^{-1}$ at 20 °C [87]). The diffusion coefficient of the unimers or aggregates was calculated using

$$D = D_{Rh6G} \times \frac{\tau_{D,Rh6G}}{\tau_D}. \quad (2)$$

The hydrodynamic radii of the unimers or aggregates, r_H, were determined using the Stokes–Einstein equation,

$$r_H = \frac{k_B T}{6\pi\eta D}, \quad (3)$$

with η being the viscosity of water and k_B being the Boltzmann constant.

As the sample temperature could not be determined during the measurements, the temperature calibration was carried out ex situ. The sample temperature was installed using a heating chamber (Carl Zeiss Jena GmbH) with a custom-made metal lid connected to a Julabo F12-MC thermostat. To avoid heat losses, the objective was additionally heated by an objective heater (Carl Zeiss Jena GmbH). With this set-up, stable and reproducible sample temperatures between 19 and 46 °C could be realized.

For the FCS experiments, aqueous solutions of 0.5 and 5 mg/mL of the nonlabeled polymer were prepared. Aqueous stock solutions of the corresponding fluorescence-labeled polymer were prepared, and a small amount was added to the solution of the nonlabeled polymer, such that the concentration of the fluorophore in the final solution was 20–100 nM. The

Table 1 Analytical data of poly (2-oxazoline) homo- and copolymers

Polymer	M^{theor}(g/mol)	M^{NMR} (g/mol)[a]	$Đ$[b]	Yield (%)
P*i*PrOx$_{25}$	2,925	2,929	1.24	75
P*i*PrOx$_{40}$	4,620	4,626	1.19	86
P*i*PrOx$_{50}$	5,750	5,758	1.17	78
P*n*PrOx$_{25}$	2,925	2,929	1.30	78
P*n*PrOx$_{50}$	5,750	5,758	1.40	86
P(*n*PrOx$_{25}$-*b*-*i*PrOx$_{25}$)	5,750	5,758	1.36	86
P(*i*PrOx$_{48}$NOx$_2$)$_{grad}$	5,918	5,926	1.19	77
P(*i*PrOx$_{46}$NOx$_4$)$_{grad}$	6,086	6,094	1.19	80

$Đ=M_w/M_n$ is the dispersity index

[a]Determined by ^{1}H-NMR end group analysis

[b]Determined by GPC

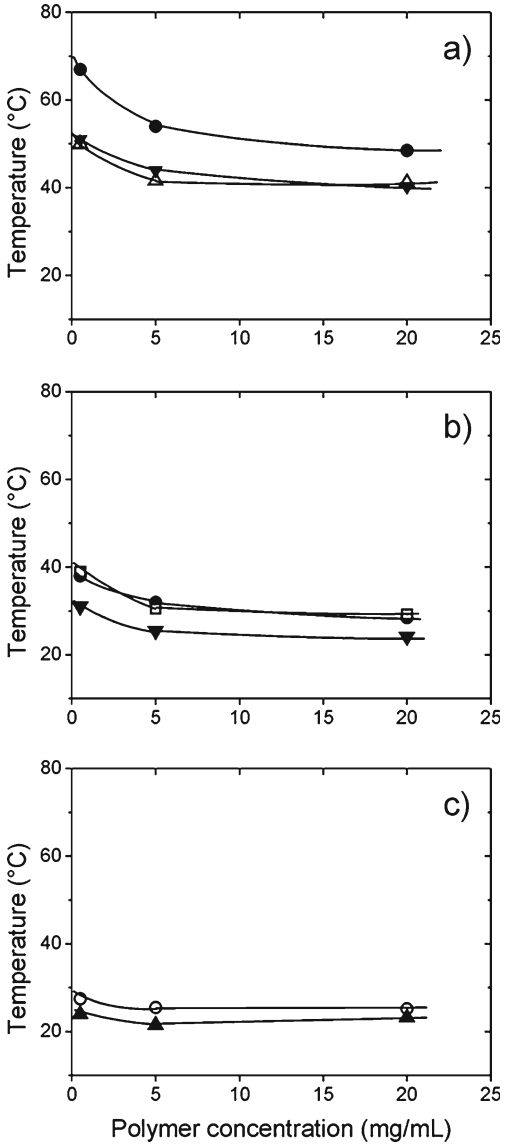

Fig. 1 Low concentration part of the LCST type phase diagrams of **a** P*i*PrOx$_{25}$ (*filled circles*), P*i*PrOx$_{40}$ (*open up-pointing triangles*), and P*i*PrOx$_{50}$ (*filled down-pointing triangles*), **b** P*n*PrOx$_{25}$ (*filled circles*), P*n*PrOx$_{50}$ (*filled down-pointing triangles*), P(*i*PrOx$_{25}$-*b*-*n*PrOx$_{25}$; *open squares*), and **c** P[*i*PrOx$_{48}$NOx$_2$]$_{grad}$ (*open circles*) and P[*i*PrOx$_{46}$-NOx$_4$]$_{grad}$ (*filled up-pointing triangles*) in H_2O. The cloud points were determined using turbidimetry. The experimental error of all temperatures is ±1 °C. The *lines* are guides to the eye

final solution was freshly filtered (Rotilabo syringe filter; pore diameter, 0.45 μm) before the experiments. Higher concentrations could not be addressed, because sedimentation of large aggregates blocked the incident and fluorescent light and thus resulted in deterioration of the FCS signal, which is measured from below.

Small-angle neutron scattering

SANS experiments were carried out at the KWS-1 instrument of the JCNS outstation at the FRM II,

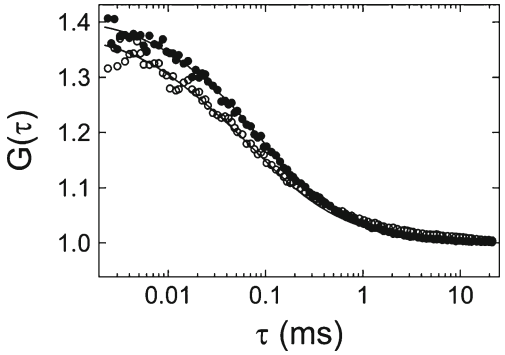

Fig. 2 FCS correlation functions of aqueous solutions with 5 mg/mL: P*i*PrOx$_{40}$ at 34.5 °C (*filled circles*) and 43.5 °C (*empty circles*). The *lines* are fits of Eq. 1 for a single decay at 34.5 °C and two decays at 43.5 °C

Garching, Germany. For the experiments, a wavelength λ=0.7 nm ($\Delta\lambda/\lambda$=20%) and sample-detector distances (SDD) of 1.71 and 7.70 m were used, which resulted in a q range of 0.03–2.1 nm^{-1}. The detector is a ^{6}Li glass scintillation detector with an active area of 60×60 cm [88]. Solutions of 20 mg/mL in D_2O were used. After each temperature change, the samples were equilibrated for 6 min. Exposure times were 5 min at SDD=1.71 m and 15 min at SDD=7.70 m. The samples were mounted in standard Hellma glass cuvettes with a light path of 2 mm in an oven. The oven was an aluminum sample holder with a plastic covering. The temperature was controlled by a heating circulator. We note that sedimentation of aggregates was not an issue in SANS experiments. The beam hits the sample from the side (and not from below as in the FCS experiments) and has a large diameter (7 mm). Moreover, possible sedimentation was very slow because the cuvette is very thin. Poly(methyl methacrylate) was used to determine the detector sensitivity. The scattering of boron carbide was used for correcting the intensities for dark current and background. The scattering of D_2O and the empty cell were subtracted from the sample scattering, taking the transmissions into account. The resulting intensities were azimuthally averaged. Good agreement was found in the overlap region of the curves measured at the two SDDs. All data reduction was performed with the software QtiKWS provided by JCNS.

Model fitting of the SANS curves

Model fitting was carried out using the NIST software implemented in Igor Pro [89]. In all curves, two contributions were observed: form factor scattering at high q values from the unimers and forward scattering from large aggregates at low q values. Two functions were used to model the single-chain scattering, $I_{chain}(q)$. For P*i*PrOx$_{50}$, P(*i*PrOx$_{25}$-*b*-

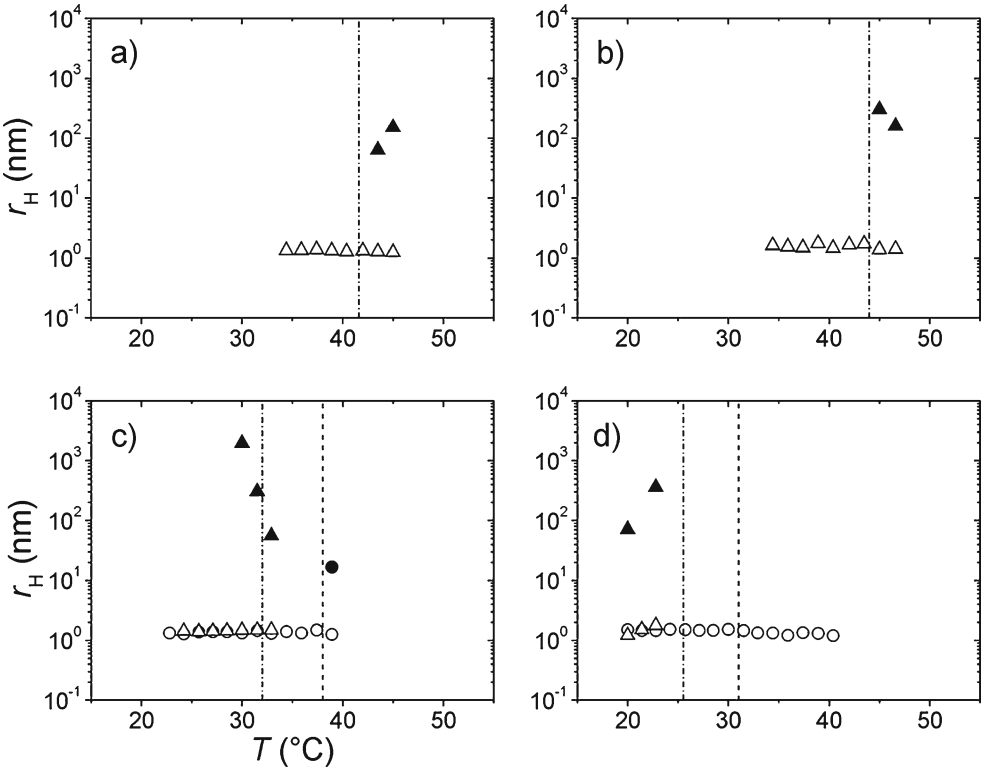

Fig. 3 Hydrodynamic radii of POx unimers and aggregates as determined by FCS. **a** P*i*PrOx$_{40}$, **b** P*i*PrOx$_{50}$, **c** P*n*PrOx$_{25}$, and **d** P*n*PrOx$_{50}$. *Circles*, 0.5 mg/mL and *triangles*, 5 mg/mL, both in H_2O. *Open symbols*, unimers and *closed symbols*, aggregates. The *vertical dashed* and *dashed-dotted lines* indicate the cloud points from turbidimetry at 0.5 and 5 mg/mL, respectively

*n*PrOx$_{25}$) and poly[(2-*iso*-propyl-2-oxazoline)$_{48}$-(2-*n*-nonyl-2-oxazoline)$_2$]$_{grad}$ (P[*i*PrOx$_{48}$NOx$_2$]$_{grad}$), a Debye function was used:

$$I_D(q) = I_D^0(\rho_{pol} - \rho_{D_2O})^2 \times \frac{2[e^{-q^2R_g^2} + q^2R_g^2 - 1]}{(q^2R_g^2)^2}, \quad (4)$$

where $I_D^0 = N_D V_D^2$, N_D denoting the number of polymer chains and V_D their respective volume, ρ_{pol} and ρ_{D2O} the scattering length densities of the polymer and of D_2O, and R_g the radius of gyration of the chain. For the scattering length densities, the following values were fixed during the fitting procedure: $r_{D_2O} = 6.36 \times 10^{-10}\text{cm}^{-2}$ and $r_{pol} = 0.20 \times 10^{-10}\text{cm}^{-2}$, where the latter value was calculated from the polymer mass density of 1.05 g/cm^3 [90]. For poly[(2-*iso*-propyl-2-oxazoline)$_{46}$-(2-*n*-nonyl-2-oxazoline)$_4$]$_{grad}$ (P[*i*PrOx$_{46}$NOx$_4$]$_{grad}$), instead of $I_D(q)$, the sphere form factor describing homogeneous spheres was used to model the scattered intensity:

$$I_S(q) = I_S^0(\rho_{pol} - \rho_{D_2O})^2 \times \left(\frac{3[\sin(qR) - qR\cos(qr)]}{(qR)^3}\right)^2, \quad (5)$$

where $I_S^0 = N_S V_S^2$, N_S denoting the number of spheres and V_S and R their respective volume and radius. The size distribution of the spheres was modeled by a Schultz–Zimm distribution which has the functional form

$$f(R) = (z-1)^{z-1}x^z \times \frac{\exp[-(z+1)x])}{R_{avg}\Gamma(z+1)}, \quad (6)$$

Here, R_{avg} denotes the average radius, $x = R/R_{avg}$ and $z = 1/p^2 - 1$ with $p = \sigma/R_{avg}$ where σ is the standard deviation of the radius.

In addition to the single-chain scattering described by $I_D(q)$ and $I_s(q)$, forward scattering due to large aggregates was observed in many cases. This contribution, $I_{agg}(q)$, was modeled using Eq. 5 with a significantly higher value of R than the unimer R_g or R. The total intensity was thus modeled by

$$I(q) = I_{chain}(q) + I_{agg}(q) + \text{bkg}, \quad (7)$$

where bkg is the incoherent background. The background was left free during the fitting and gave nearly the same value in all fits (~0.25 cm^{-1}) which is consistent with the calculated value (0.27 cm^{-1}).

Results and discussion

Synthesis

The monomers, *i*PrOx and *n*PrOx were obtained following the procedure by Seeliger et al. [91]. By living cationic ring-

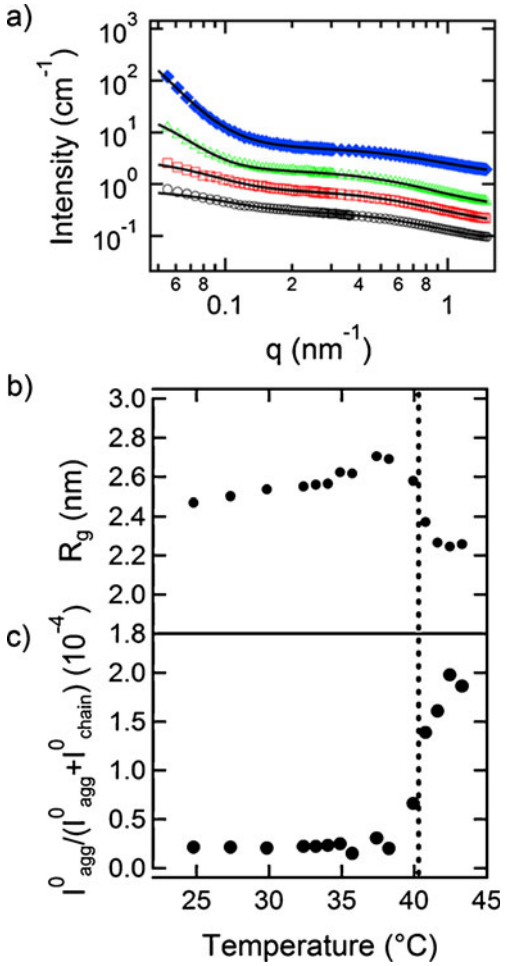

Fig. 4 SANS results of sample P*i*PrOx$_{50}$ at 20 mg/mL in D_2O. **a** Representative scattering curves: *open circles*, 24.8 °C; *open squares*, 32.4 °C; *open triangles*, 37.4 °C, *closed diamonds*, 41.6 °C. The *solid lines* are model fits, see text. For clarity, the intensities are shifted by factors of 2, 4, and 16. **b** Radius of gyration of the single chains. **c** Normalized forward scattering intensity of the large aggregates normalized by total forward scattering, see text. In (**b**) and (**c**), the error bars are smaller than the symbol size. The vertical dashed lines in (**b**) and (**c**) mark the cloud point from turbidimetry in H_2O

opening polymerization, the respective polymers, P*i*PrOx$_n$ and P*n*PrOx$_n$, with n=25, 40, and 50 were obtained in high yields and low dispersities. Furthermore, one P(*i*PrOx$_n$-*b*-*n*PrOx$_m$) block copolymer with n, m=25 was obtained by sequential monomer addition and two gradient copolymers of *i*PrOx with NOx with a monomer feed composition of 48:2 and 46:4 were obtained by the one-shot copolymerization technique. All polymerization reactions were carried out using microwave-assisted synthesis as reported before [12, 56] with MeOTf as the initiator and piperazine as the terminating agent. For the study of the polymer aggregation near the cloud point, small portions of the polymers were additionally labeled with the rather hydrophilic fluorescence label TRITC via a polymer analogue coupling reaction on the secondary amine function [28]. The homo- and copolymerization reactions are summarized in Scheme 1. The analytical data of the synthesized polymers are summarized in Table 1.

This set of defined polymers enables us to study the diffusion of unimers as well as their aggregation behavior around the cloud point by FCS. We vary the average degree of polymerization, n, the 2-substitution and thus the hydrophobicity (*iso*-propyl-, *n*-propyl-, and *n*-nonyl-) as well as the polymer composition, n/m. By means of SANS, we gained more insight into the polymer conformation and the aggregation behavior.

Homopolymers P*i*PrOx$_n$ and P*n*PrOx$_n$

The cloud points of P*i*PrOx$_n$ and P*n*PrOx$_n$ homopolymers with n between 25 and 50 were determined by turbidimetry at concentrations of 0.5, 5, and 20 mg/mL in aqueous solution (Fig. 1a, b). As expected, they were found to depend both on the degree of polymerization, n, and on the concentration, c, as shown in Fig. 1a. The cloud points decrease with increasing concentration and with increasing degree of polymerization. The values of P*i*PrOx$_n$ are above 40 °C, whereas the ones of P*n*PrOx$_n$ are significantly lower (24–38 °C, Fig. 1b). Thus, the latter is more hydrophobic, as expected from the extended nature of the side group in P*n*PrOx$_n$. The transitions are very sharp, usually of the order of 1–2 K.

Temperature-resolved FCS allowed us to characterize the aggregation behavior around the cloud point. As reliable measurements could only be performed in the temperature range up to ~50 °C, we investigated solutions of P*i*PrOx$_{40}$ and P*i*PrOx$_{50}$ at 5 mg/mL. In these solutions, only a very minor fraction of chains (1 out of 1,000) is labeled with TRITC at one chain terminus. The aggregation behavior is thus not expected to be perturbed by a possible interaction between the dyes. For both polymers, a single, fast decay is present in the FCS autocorrelation functions (Fig. 2). The hydrodynamic radii derived using Eq. 1–3 are found to be r_H=1–2 nm, and are attributed to unimers, i.e. single dissolved polymers (Fig. 3), in consistency with our previous studies on POx copolymers [28–30]. Above the cloud point, the solutions are turbid. However, unimers are still detectable, and an additional slow decay is observed in the FCS autocorrelation functions. The decay times calculate to r_H= 60–300 nm with amplitudes between 0.05 and 0.30 and are attributed to the formation of large polymer aggregates. The aggregates dissolve completely upon cooling, the process was found to be reversible. Similar aggregate formation has frequently been observed in PNIPAM homopolymer solutions [92]. Interestingly, the hydrodynamic radius of the polymer unimers stays unchanged when the cloud point is crossed, i.e. the collapse of single chains cannot be detected by FCS.

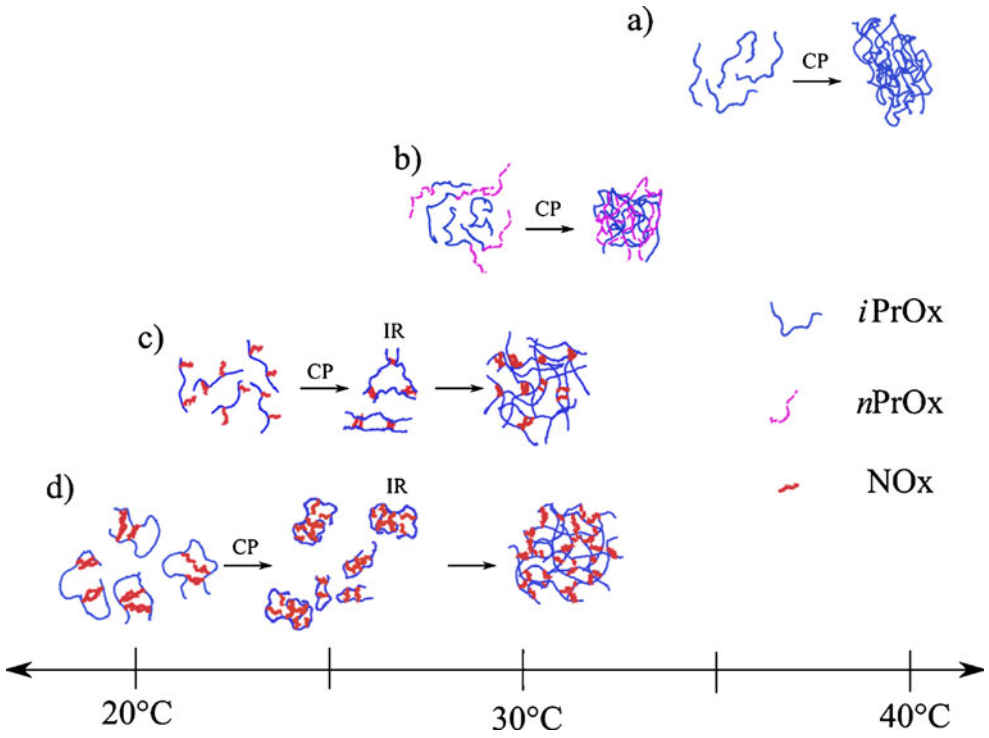

Scheme 2 Schematics of the temperature-dependent aggregation behavior of P*i*PrOx homopolymers (**a**), P(*i*PrOx$_{25}$-*b*-*n*PrOx$_{25}$) diblock copolymers (**b**), P[*i*PrOx$_{48}$NOx$_2$]$_{grad}$ (**c**), and P[*i*PrOx$_{46}$NOx$_4$]$_{grad}$ gradient copolymers (**d**). The different colors and line types indicate the monomer type. CP stands for cloud point, IR for the intermediate regime

Investigation of P*n*PrOx$_n$ homopolymers did not show as clear results as that. For P*n*PrOx$_{25}$ at 0.5 mg/mL, the same behavior as for P*i*PrOx$_{40}$ and P*i*PrOx$_{50}$ is observed, namely aggregate formation above the cloud point (38 °C) with the aggregates having a hydrodynamic radius of 17 nm (amplitude, 0.026), thus smaller than in the case of the two P*i*PrOx$_n$ homopolymers (Fig. 3c). At 5 mg/mL, the cloud point (32 °C) is already quite close to room temperature, and very large aggregates are already observed at 30 °C (amplitude increases with temperature from 0.04 to 0.28). The cloud points of P*n*PrOx$_{50}$ are much lower (25.5 and 31 °C for 5 and 0.5 mg/mL, respectively) than the ones of P*n*PrOx$_{25}$, and the aggregation behavior is different (Fig. 3d): At 0.5 mg/mL, no aggregates could be detected even far above the cloud point, whereas at 5 mg/mL, aggregates were already present at 20 °C (amplitudes, 0.06 and 0.12), i.e., below the cloud point. For both P*n*PrOx$_n$ homopolymers, the aggregates did not dissolve rapidly upon cooling.

SANS measurements allowed us to gain more insight into the mechanism of aggregation around the cloud points. Temperature-resolved studies were carried out on a 20-mg/mL solution of P*i*PrOx$_{50}$ in D_2O. This relatively high concentration was necessary to achieve a sufficient scattering signal. Due to the different geometry of the SANS experiment compared to FCS, segregation was not an issue. The use of D_2O instead of H_2O has in other systems only resulted in minor shifts of the phase transition temperatures but has shown the same aggregation behaviors. Representative SANS curves at temperatures below and above the cloud point (40.0 °C) are given in Fig. 4a. At all temperatures, they show a smooth decay above ~0.2 nm^{-1} which is due to single chain scattering. At low q values, an additional scattering contribution is observed which increases in amplitude upon heating through the cloud point. We attribute this contribution to large aggregates formed by collapsed polymers. Over the entire temperature range, the curves could very well be modeled by the sum of a Debye function (Eq. 4), describing the scattering of ideal polymer coils, and a sphere form factor to model the aggregates (Eq. 5). It was not necessary to include a structure factor resulting from interparticle interaction; in fact, tests of several structure factors did not improve the fitting quality. The resulting radius of gyration of the unimers (Fig. 4b) increases weakly from ~2.5 nm at 25 °C to 2.7 nm at 38.2 °C. Above, it decreases rapidly and reaches 2.3 nm at 43.2 °C, i.e., a certain fraction of the polymers is present as unimers which collapse.

Assuming that D_2O is a theta solvent for P*i*PrOx$_{50}$ below the cloud point, R_g is expected at $R_g = b(N/6)^{0.5} =$ 1.07 nm (with b=0.37 nm [66]). This value is in consistency with the measured value. The measured radius of gyration is of the same order of magnitude as the one found in the FCS experiment at 5 mg/mL. To determine the origin of the increase of R_g with temperature, we consider the fitted forward intensity. It increases with temperature when approaching the cloud point (not shown), i.e., the increase of R_g with temperature is due to aggregation of few unimers. The radius of the large aggregates cannot be determined precisely due to the limited q range of our experiment, but we consistently obtained 50–60 nm from the fits.

To estimate the fraction of large aggregates as a function of temperature, we plot the relative forward scattering intensity of their scattering contribution, normalized by the total forward scattering intensity, $I_{agg}^{0}/(I_{agg}^{0}+I_{chain}^{0})$ (Fig. 4c). We note that V_s and V_D only change weakly in the temperature range studied, thus the intensity ratio is a measure of $N_{agg}/(N_{agg}+N_{chain})$. It increases steeply at the cloud point, i.e., above this temperature large aggregates are formed in significant number.

The SANS results corroborate our findings from FCS that the polymers are dissolved as unimers, which form small aggregates as the cloud point is approached and which collapse above the cloud point. A certain fraction of these collapsed polymers form large aggregates above the cloud point (Scheme 2a).

A diblock copolymer P(*i*PrOx$_{25}$-*b*-*n*PrOx$_{25}$)

For a diblock copolymer with two thermo-responsive blocks P*i*PrOx and P*n*PrOx, it is expected that the block copolymer is completely water-soluble below the cloud point of P*n*PrOx and that micelles are formed as the cloud point of P*n*PrOx is crossed which consist of a water-insoluble P*n*PrOx core and a water-soluble P*i*PrOx shell, similar to poly(2-methyl-2-oxazoline-*block*-2-*n*-nonyl-2-oxazoline) [66]. When the cloud point of P*i*PrOx is crossed, the shell will also become hydrophobic, and the micelles will form large aggregates. A two-step aggregation behavior is thus expected for a P(*n*PrOx$_{25}$-*b*-*i*PrOx$_{25}$) diblock copolymer.

Turbidimetry, however, shows a behavior very similar to the one of P*n*PrOx$_{25}$ (Fig. 1). The cloud point lies between 28.5 and 38 °C for concentrations between 20 and 0.5 mg/mL, i.e., already at these temperatures, large aggregates which scatter the light are formed. With FCS, no micelles could be detected either (Fig. 5): at 5 mg/mL, aggregates with a hydrodynamics radius larger than 200 nm are formed right above the cloud point (amplitude, 0.13–0.17). In contrast, in the accessible temperature range, no aggregates could be detected at 0.5 mg/mL. In this sample, the unimer size could not be determined reliably because it may contain free TRITC.

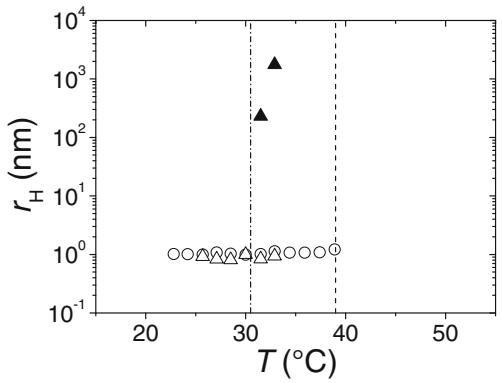

Fig. 5 Hydrodynamic radii of P(*i*PrOx$_{25}$-*b*-*n*PrOx$_{25}$) determined using FCS. Same symbols as in Fig. 2

SANS at 20 mg/mL in D_2O confirmed that no micelles are formed at the cloud point of the P*n*PrOx$_{25}$ block (28.5 °C; Fig. 6a). The scattering curves could again be fitted with the Debye model, i.e., $I_{chain}(q)=I_D(q)$. Above 27.3 °C, an additional scattering contribution from large aggregates is observed, which is again modeled by a sphere form factor. The radius of gyration of the unimers is 2.4 nm up to 29 °C (Fig. 6b). In contrast to the P*i*PrOx$_{50}$ homopolymer, it is not temperature-dependent. Above 29 °C, the radius of gyration decreases to 1.7 nm at 35 °C, i.e., the unimers collapse at the cloud point of the more hydrophobic P*n*PrOx$_{25}$ block. Above 29 °C, the collapsed diblock

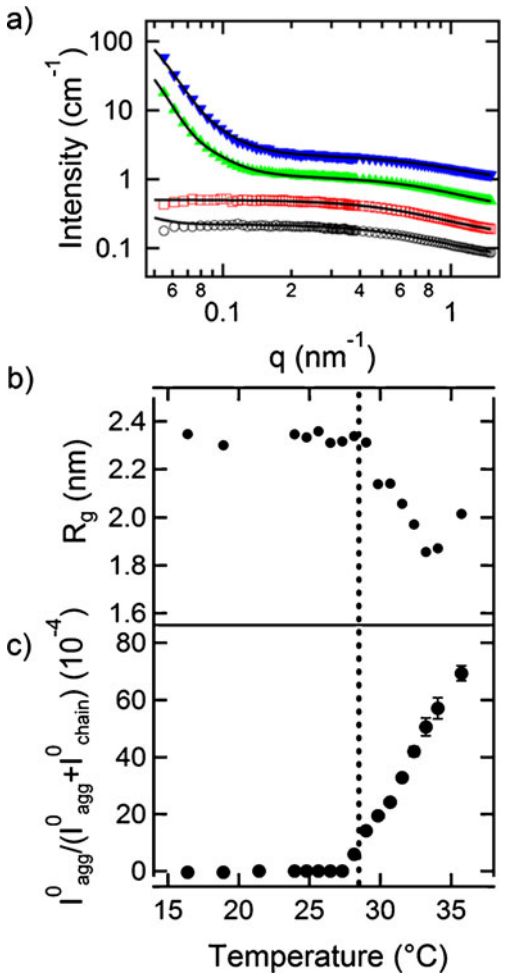

Fig. 6 SANS results of P(*i*PrOx$_{25}$-*b*-*n*PrOx$_{25}$) at 20 mg/mL in D_2O. **a** Representative scattering curves: *open circles*, 16.4 °C; *open squares*, 24.8 °C; *closed triangles up*, 33.2 °C; and *closed down-pointing triangles*, 37.4 °C. The *full lines* are model fits, see text. The intensities are shifted by factors of 2, 4, and 16. **b** Radius of gyration of the unimers. **c** Normalized forward scattering intensity of the large aggregates normalized by total forward scattering, see text. The *vertical dashed lines* in (**b**) and (**c**) mark the cloud point from turbidimetry in H_2O

copolymers form aggregates larger than 50 nm, thus far too big to be attributed to core-shell micelles. Above 27.3 °C, the number fraction of aggregates increases steadily (Fig. 6c), thus above the cloud point determined by turbidimetry, large aggregates are formed in significant number. We conclude that, contrary to expectation, SANS does not give any hint to the presence of micelles above the cloud point of P*n*PrOx$_{25}$ which are expected to have a micellar radius of ~5–10 nm [66]. Instead, all methods (turbidimetry, FCS and SANS) point to the immediate formation of large aggregates at the cloud point of P*n*PrOx$_{25}$ (Scheme 2b).

Gradient copolymers P[*i*PrOx$_n$Ox]$_{grad}$

Two gradient copolymers were investigated, where, on average, out of 50 *i*PrOx monomers, two or four are replaced by (very hydrophobic) NOx monomers. We expect a lower cloud point and the formation of unimolecular micelles in which the *n*-nonyl side groups of the NOx monomers are in the core and are shielded from water by the polar backbone and the *i*PrOx monomers. Again, above the cloud point of P*i*PrOx, large aggregates containing a high number of polymers are expected with the cloud point being much lower than the ones of the P*i*PrOx homopolymers because of the NOx monomers [13].

Indeed, we found very low cloud points for the gradient copolymers (Fig. 1c). They lie between 21.5 and 27.5 °C, i.e., far below the ones of P*i*PrOx$_{50}$ (40.0–51.0 °C; Fig. 1a). The cloud points are as sharp as in the case of the P*i*PrOx$_{50}$ homopolymer.

FCS reveals a quite complex aggregation behavior for both gradient copolymers (Fig. 7). At 0.5 mg/mL, apart from the unimers having r_H=1–2 nm, small aggregates having r_H=25–30 nm are present already a few Kelvin below the cloud point. At the cloud point, the aggregates grow and reach sizes of r_H=150–250 nm. At this point, their fraction increases considerably (Fig. 7c, d). Above 27 °C, FCS measurements are not possible for P[*i*PrOx$_{48}$NOx$_2$]$_{grad}$ because of sedimentation, i.e., the formation of very large aggregates. Similar behavior—the formation of small aggregates already below the cloud point and subsequent sedimentation – is observed at 5 mg/mL (Fig. 7b, d).

The SANS curves of P[*i*PrOx$_{48}$NOx$_2$]$_{grad}$ solutions of 20 mg/mL in D_2O (Fig. 8a) are very similar to the ones of P*i*PrOx$_{50}$ (Fig. 4a), and the same model can be used for fitting (Debye functions for the unimers and spheres for the aggregates). Between 12.1 and 25.6 °C, the average radius of gyration of the unimers increases from 3.0 to 5.6 nm. R_g at temperatures far from the cloud point is close to the value of P*i*PrOx$_{50}$. Again, the forward intensity increases, i.e., the increase of R_g is due to aggregation of few chains already below the cloud point which may be promoted by the *n*-nonyl side groups. Between 25.6 and 29 °C, R_g stays at 4–6 nm and only then increases steeply.

Below the cloud point, the increase of R_g with temperature is stronger than in P*i*PrOx. We attribute it to the aggregation of a few chains which are mediated by the NOx blocks (Scheme 2c). At the cloud point, the chains/small aggregates tend to collapse because now also the P*i*PrOx monomers become hydrophobic. However, this collapse is

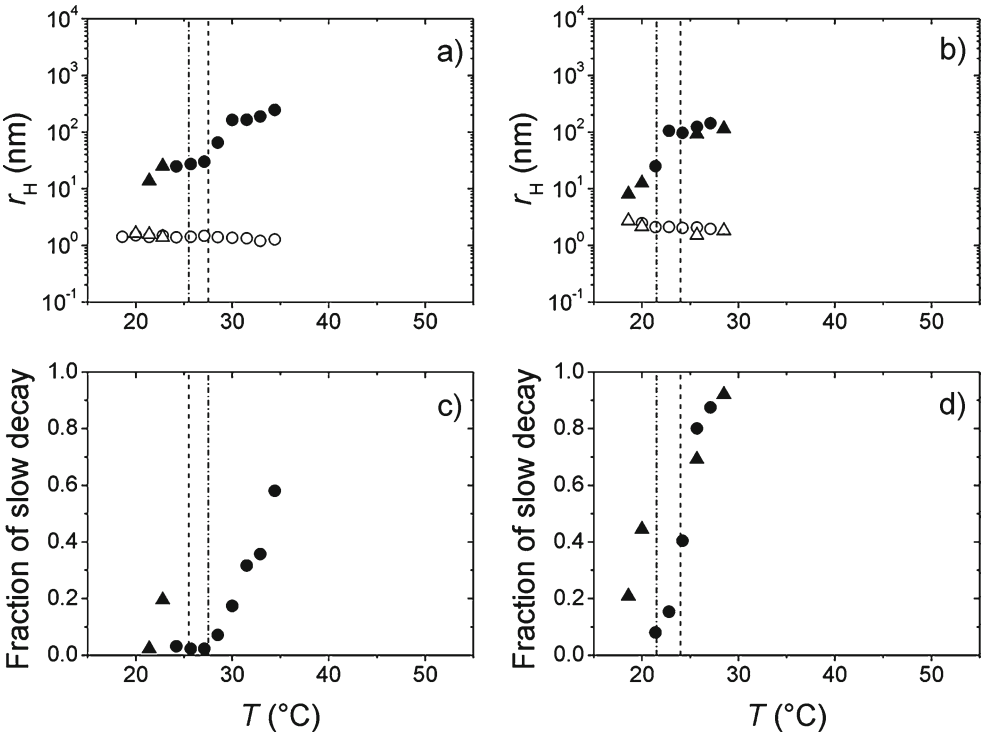

Fig. 7 Hydrodynamic radii of **a** P[*i*PrOx$_{48}$NOx$_2$]$_{grad}$ and **b** P[*i*PrOx$_{46}$NOx$_4$]$_{grad}$ determined using FCS as well as the fraction of the slow decay (**c**, **d**). Same symbols as in Fig. 2

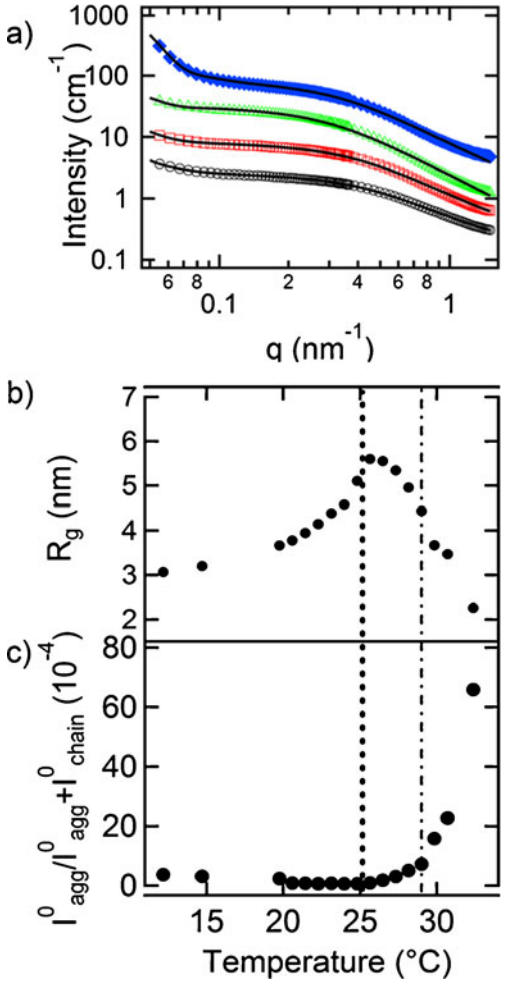

Fig. 8 SANS results of P[*i*PrOx$_{48}$NOx$_2$]$_{grad}$ at 20 mg/mL in D_2O. **a** Representative scattering curves: *open circles*, 12.2 °C; *open squares*, 20.6 °C; *open up-pointing triangles*, 24.8 °C; and *closed diamonds*, 29.0 °C. The *full lines* are model fits, see text. The intensities are shifted by factors of 2, 4, and 16. **b** Radius of gyration of the unimers. **c** Normalized forward scattering intensity of the large aggregates normalized by total forward scattering, see text. The *error bars* in (**b**) and (**c**) are smaller than the symbol size. In (**b**) and (**c**), the *vertical dashed line* marks the cloud point from turbidimetry in H_2O. The *dashed-dotted line* marks the upper limit of the intermediate aggregation regime, see text

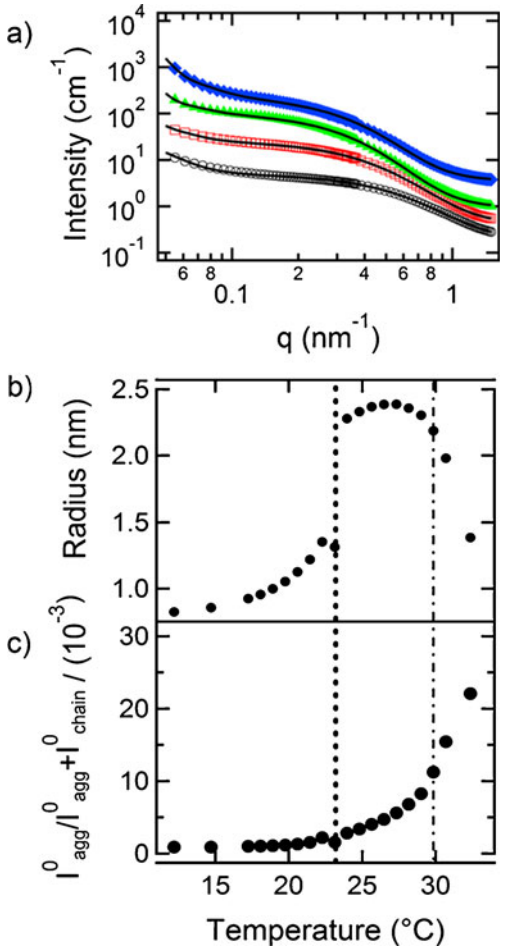

Fig. 9 SANS results of P[*i*PrOx$_{46}$NOx$_4$]$_{grad}$ at 20 mg/mL in D_2O. **a** Representative scattering curves: *open circles*, 12.2 °C; *open squares*, 20.6 °C; *open up-pointing triangles*, 24.8 °C; and *closed diamonds*, 29.0 °C. The *full lines* are model fits, see text. The intensities are shifted by factors of 2, 4, and 16. **b** Radius of unimers. **c** Normalized forward scattering intensity of the large aggregates normalized by total forward scattering, see text. The *error bars* in (**b**) and (**c**) are smaller than the symbol size. In (**b**) and (**c**), the *vertical dashed line* marks the cloud point from turbidimetry in H_2O. The *dashed-dotted line* marks the upper limit of the intermediate regime, see text

sterically hindered by the already associated chains, which are bridged by the NOx blocks. Therefore, these small aggregates, formed by few, now completely hydrophobic chains, are stable at R_g=5.6 nm up to ~29 °C. Only above this temperature, the small aggregates collapse, and a significant number of aggregates larger than 50 nm are formed. Thus an intermediate regime is encountered between 25.6 and 29 °C, similar to the observation made with FCS for lower polymer concentrations. The collapse and aggregation behavior is thus more complex than observed for the P*i*PrOx$_{50}$ homopolymer.

The SANS curves of P[*i*PrOx$_{46}$NOx$_4$]$_{grad}$ copolymers could not be fitted using the Debye function for unimers (Fig. 9a) in the q region above 0.2 nm^{-1} but instead with a form factor for homogeneous spheres (Eq. 5). This indicates a compact chain conformation, which is due to the additional hydrophobic interaction by the *n*-nonyl side groups. A possible inner structure cannot be resolved due to the low internal scattering contrast of the polymer. Together with a sphere form factor describing the aggregates, good fits could be obtained. Thus, the aggregation behavior is very similar to the one described in Ref. [93]. Intramolecular bridging of nonsoluble comonomers prevails over intermolecular association, leading to a more compact chain conformation.

Between 12.1 and 23.1 °C, the resulting sphere radius of the unimers increases from 0.8 to 1.3 nm. The unimer radius discontinuously jumps to 2.4 nm where it stays up to 30 °C. Only above this temperature, it decreases steeply. The relative number of large aggregates increases weakly between 23.1 and 30 °C and much stronger at elevated temperatures.

In the swollen state below the cloud point, the radii of the unimers are smaller than the ones of P[*i*PrOx$_{48}$NOx$_2$]$_{grad}$ because of a more compact chain conformation of P[*i*PrOx$_{46}$NOx$_4$]$_{grad}$. The higher number of NOx moieties results in intramolecular association with the *i*PrOx monomers screening the hydrophobic interactions between NOx monomers from different chains (Scheme 2d). Above the cloud point, the copolymer is hydrophobic and forms small aggregates which are stable up to 30 °C. Only above this temperature, the small aggregates collapse, and aggregates larger than 50 nm form in higher numbers (Scheme 2d). This two-step aggregation is consistent with the FCS observation at lower polymer concentration.

Summary

Due to its versatility regarding side groups and chain architecture, the POx system is ideally suited to study the aggregation behavior of thermo-responsive polymers. The cloud point varies over a wide range (here between 21 and 67 °C) which allows tailoring stimuli-responsive materials for specific applications. Moreover, POx are nontoxic and biocompatible and both P*n*PrOx and P*i*PrOx show cloud points in the physiological range.

Combining an ensemble method (turbidimetry), a quasi-single molecule method (FCS) and a scattering method (SANS), we have investigated the thermo-responsive behavior of P*i*PrOx homopolymers as well as compositionally symmetric diblock copolymers from P*i*PrOx with thermo-responsive, but slightly more hydrophobic P*n*PrOx and gradient copolymers with few very hydrophobic NOx monomers, all at concentrations between 0.5 and 20 mg/mL. In FCS, fluorescence-labeled polymers served as tracers in dilute aqueous solutions of the identical nonlabeled polymers. By means of SANS on concentrated solutions, the chain conformation and the aggregation behavior could be elucidated. The results are summarized in Scheme 2.

The P*i*PrOx homopolymers are dissolved as unimers below the cloud point, where they collapse and form large aggregates. The aggregate formation is fully reversible. In contrast, the P*n*PrOx homopolymers have much lower cloud points, and the aggregates do not fully dissolve upon cooling which we attribute to side chain crystallization occurring above the cloud point. The behavior of the thermo-responsive P*i*PrOx and P*n*PrOx homopolymers is reminiscent of the one encountered with other thermo-responsive homopolymers, such as PNIPAM [7, 10]. The cloud points of both, P*i*PrOx and P*n*PrOx, depend strongly on concentration (especially below 5 mg/mL) and on the degree of polymerization.

The diblock copolymer behaves in the same way as the homopolymer with the lower cloud point. Contrary to our expectations, no micelles are formed between the two cloud points, but large aggregates are formed right away at the cloud point of P*n*PrOx.

The behavior of the gradient copolymers is governed by the association mediated by the strongly hydrophobic *n*-nonyl side groups: even below the cloud point of the P*i*PrOx main chain, intra- or intermolecular association hinder the collapse and a significant number of large aggregates are only formed within a few Kelvin above the cloud point. For P[*i*PrOx$_{48}$NOx$_2$]$_{grad}$, already below the cloud point small aggregates form which persist above the cloud point. Only a few Kelvin above the cloud point large aggregates start to dominate.

The aggregation behavior of P[*i*PrOx$_{46}$NOx$_4$]$_{grad}$ is similar to the one of P[*i*PrOx$_{48}$NOx$_2$]$_{grad}$ with small aggregates forming below the cloud point which stay stable up to a few Kelvin above the cloud point. The difference is that the NOx groups mediating the interaction between the chains now find more partners within the same chain; thus, also compact unimers are present where the NOx monomers are shielded from hydrophobic interaction with water by the *i*PrOx monomers. Therefore, the intermediate regime is more pronounced than for P[*i*PrOx$_{48}$NOx$_2$]$_{grad}$.

We conclude that the P*i*PrOx system offers manifold possibilities to tune the cloud point. The copolymerization with more hydrophobic monomers results in an increased complexity of the collapse transition.

Acknowledgments We thank E. T. Hoppe for assistance with FCS and fruitful discussions. We gratefully acknowledge financial support by the DFG (Pa771/6-2, Jo287/4-3).

References

1. Hoffman AS (1987) J Control Release 6:297
2. Coughlan DC, Quilty FP, Corrigan OI (2004) J Control Release 98:97
3. Schmaljohann D (2006) Adv Drug Delivery Rev 58:1655
4. Feil H, Bae YH, Feijen J, Kim SW (1991) J Membrane Sci 64:283
5. Park YS, Ito Y, Imanishi Y (1998) Langmuir 14:910
6. Nykänen A, Nuopponen M, Laukkanen A, Hirvonen SP, Rytelä M, Turunen O, Tenhu H, Mezzenga R, Ikkala O, Ruokolainen J (2007) Macromolecules 40:5827
7. Schild HG (1992) Progr Polym Sci 17:163
8. Lin SY, Chen KS, Run-Chu L (1999) Polymer 40:2619
9. Katsumoto Y, Tanaka T, Sato H, Ozaki Y (2002) J Phys Chem A 106:3429
10. Okada Y, Tanaka F (2005) Macromolecules 38:4465
11. Foreman MB, Coffman JP, Murcia MJ, Cesana S, Jordan R, Smith GS, Naumann CA (2003) Langmuir 19:326
12. Huber S, Hutter N, Jordan R (2008) Colloid Polym Sci 286:1653
13. Park JS, Kataoka K (2007) Macromolecules 40:3599
14. Park JS, Kataoka K (2006) Macromolecules 39:6622
15. Hoogenboom R, Thijs HML, Jochems MJHC, van Lankvelt BM, Fijten MWM, Schubert US (2008) Chem Commun 44:5758
16. Luxenhofer R, Schulz A, Roques C, Li S, Bronich TK, Batrakova EV, Jordan R (2010) Biomaterials 31:4972

17. Zarka MT, Nuyken O, Weberskirch R (2004) Macromol Rapid Commun 25:858
18. Cesana S, Auernheimer J, Jordan R, Kessler H, Nuyken O (2006) Macromol Chem Phys 207:183
19. Taubmann C, Luxenhofer R, Cesana S, Jordan R (2005) Macromol Biosci 5:603
20. Cesana S, Kurek A, Baur MA, Auernheimer J, Nuyken O (2007) Macromol Rapid Commun 28:608
21. Gress A, Völkel A, Schlaad H (2007) Macromolecules 40:7928
22. Luxenhofer R, Jordan R (2006) Macromolecules 39:3509
23. Persigehl P, Jordan R, Nuyken O (2000) Macromolecules 33:6977
24. Kotré T, Nuyken O, Weberskirch R (2002) Macromol Rapid Commun 23:871
25. Krause JO, Zarka MT, Anders U, Weberskirch R, Nuyken O, Buchmeiser MR (2003) Angew Chem Int Ed 42:5965
26. Zarka MT, Nuyken O, Weberskirch R (2003) Chem Eur J 9:3228
27. Nuyken O, Weberskirch R, Kotré T, Schönfelder D, Wörndle A (2003) In: Buchmeiser M (ed) Polymeric materials in organic synthesis and catalysis. Wiley, Weinheim, pp 277–304
28. Bonné TB, Lüdtke K, Jordan R, Štěpánek P, Papadakis CM (2004) Colloid Polym Sci 282:833
29. Bonné TB, Lüdtke K, Jordan R, Papadakis CM (2007) Macromol Chem Phys 208:1402
30. Bonné TB, Papadakis CM, Lüdtke K, Jordan R (2007) Colloid Polym Sci 285:491
31. Velander WH, Madurawe RD, Subramanian A, Kumar G, Sinai-Zingde G, Riffle JS, Orthner CL (1992) Biotechnol Bioengin 39:1024
32. Woodle MC, Engbers CM, Zalipsky S (1994) Bioconjug Chem 5:493
33. Lasic DD, Needham D (1995) Chem Rev 95:2601
34. Zalipsky S, Hansen CB, Oaks JM, Allen TM (1996) J Pharmaceut Sci 85:133
35. Luxenhofer R, Sahay G, Schulz A, Alakhova D, Jordan R, Kabanov AV (2011) J Control Release 153:73
36. Gaertner FC, Luxenhofer R, Blechert B, Jordan R, Essler M (2007) J Control Release 119:291
37. Hoogenboom R (2009) Angew Chem Int Ed 48:7978
38. Schlaad H, Diehl C, Gress A, Meyer M, Demirel AL, Nur Y, Bertin A (2010) Macromol Rapid Commun 31:511
39. Tong J, Zimmermann MC, Li S, Yi X, Luxenhofer R, Jordan R, Kabanov AV (2011) Biomaterials 32:3654
40. Manzenrieder F, Luxenhofer R, Retzlaff M, Jordan R, Finn MG (2011) Angew Chem Int Ed 50:2601
41. Tong J, Luxenhofer R, Yi X, Jordan R, Kabanov AV (2010) Mol Pharmaceutics 7:984
42. Purrucker O, Förtig A, Jordan R, Tanaka M (2004) ChemPhysChem 5:327
43. Purrucker O, Förtig A, Lüdtke K, Jordan R, Tanaka M (2005) J Am Chem Soc 127:1258
44. Lüdtke K, Jordan R, Hommes P, Nuyken O, Naumann CA (2005) Macromol Biosci 5:384
45. Seitz PC, Reif MD, Konovalov OV, Jordan R (2009) ChemPhysChem 10:2876
46. Purrucker O, Förtig A, Jordan R, Sackmann E, Tanaka M (2007) Phys Rev Lett 98:078102
47. Garg S, Rühe J, Lüdtke K, Jordan R, Naumann CA (2007) Biophys J 92:1263
48. Purrucker O, Gönnenwein S, Förtig A, Jordan R, Rusp M, Bärmann M, Moroder L, Sackmann E, Tanaka M (2007) Soft Matter 3:333
49. Lüdtke K, Jordan R, Furr N, Garg S, Forsythe K, Naumann CA (2008) Langmuir 24:5580
50. Deverall MA, Garg S, Lüdtke K, Jordan R, Rühe J, Naumann CA (2008) Soft Matter 4:1899
51. Siegel AP, Murcia MJ, Johnson M, Reif M, Jordan R, Rühe J, Naumann CA (2010) Soft Matter 6:2723
52. Seitz P, Reif M, Yashikawa K, Jordan R, Tanaka M (2011) J Phys Chem B 115:2256
53. Lin P, Clash C, Pearce EM, Kwei TK, Aponte MA (1988) J Polym Sci Part B: Polym Phys 26:603
54. Christova D, Velichkova R, Loos W, Goethals EJ, Du Prez F (2003) Polymer 44:2255
55. Diehl C, Schlaad H (2009) Macromol Biosci 9:157
56. Huber S, Jordan R (2008) Colloid Polym Sci 286:395
57. Hoogenboom R, Lambermont-Thijs HML, Jochems MJHC, Hoeppener S, Guerlain C, Fustin CA, Gohy JF, Schubert US (2009) Soft Matter 5:3590
58. Park JS, Akiyama Y, Winnik FM, Kataoka K (2004) Macromolecules 37:6786
59. Obeid R, Maltseva E, Thünemann AF, Tanaka F, Winnik FM (2009) Macromolecules 42:2204
60. Zhang N, Huber S, Schulz A, Luxenhofer R, Jordan R (2009) Macromolecules 42:2215
61. Zhang N, Steenackers M, Luxenhofer R, Jordan R (2009) Macromolecules 42:5345
62. Hutter NA, Reitinger A, Zhang N, Steenackers M, Williams OA, Garrido JA, Jordan R (2010) PhysChemPhys 12:4360
63. Hutter NA, Steenackers M, Reitinger A, Williams OA, Garrido JA, Jordan R (2011) Soft Matter 7:4861
64. Weber C, Becer CR, Guenther W, Hoogenboom R, Schubert US (2010) Macromolecules 43:160
65. Diehl C, Schlaad H (2009) Chem Eur J 15:11469
66. Ivanova R, Komenda T, Bonné TB, Lüdtke K, Mortensen K, Pranzas PK, Jordan R (2008) Macromol Chem Phys 209:2248
67. Zettl H, Häfner W, Böker A, Schmalz H, Lanzendörfer M, Müller AHE, Krausch G (2004) Macromolecules 37:1917
68. Zettl H, Zettl U, Krausch G, Enderlein J, Ballauff M (2007) Phys Rev E 75:061804
69. Sukhishvili SA, Chen Y, Müller JD, Gratton E, Schweizer KS, Granick S (2000) Nature 406:146
70. Sukhishvili SA, Chen Y, Müller JD, Gratton E, Schweizer KS, Granick S (2002) Macromolecules 25:1776
71. Zhao J, Granick S (2004) J Am Chem Soc 126:6242
72. Zhao J, Granick S (2007) Macromolecules 40:1243
73. Gianneli M, Beines PW, Roskamp RF, Koynov K, Fytas G, Knoll W (2007) J Phys Chem C 111:13205
74. Raccis R, Roskamp R, Hopp I, Menges B, Koynov K, Jonas U, Knoll W, Butt H-J, Fytas G (2011) Soft Matter 7:7042
75. Zustiak SP, Boukari H, Leach JB (2010) Soft Matter 6:3609
76. Schuch H, Klingler J, Rossmanith P, Frechen T, Gerst M, Feldthusen J, Müller AHE (2000) Macromolecules 33:1734
77. Colombani O, Ruppel M, Schubert F, Zettl H, Pergushov DV, Müller AHE (2007) Macromolecules 40:4338
78. Loos K, Böker A, Zettl H, Zhang M, Krausch G (2005) Macromolecules 38:873
79. Erhardt R, Böker A, Zettl H, Kaya H, Pyckhout-Hintzen W, Krausch G, Abetz V, Müller AHE (2001) Macromolecules 34:1069
80. Humpolíčková J, Procházka K, Hof M, Tuzar Z, Špírková M (2003) Langmuir 19:4111
81. Cherdhirankorn T, Harmandaris V, Juhari A, Voudouris P, Fytas G, Kremer K, Koynov K (2009) Macromolecules 42:4858
82. Cherdhirankorn T, Floudas G, Butt H-J, Koynov K (2009) Macromolecules 42:9183
83. Best A, Pakula T, Fytas G (2005) Macromolecules 38:4539
84. Casoli A, Schönhoff M (2001) Biol Chem 382:363
85. Witte H, Seeliger W (1974) Liebigs Ann Chem 6:996
86. Widengren J, Mets U, Rigler R (1995) J Phys Chem 99:13368
87. Magde D, Elson EL, Webb WW (1974) Biopolymers 13:29

88. Engels R, Clemens U, Kemmerling G, Nöldgen H, Schelten (2009) Nucl Instrum Methods Phys Res Sect A 604:147
89. Kline SR (2006) J Applied Crystallogr 39:895
90. Litt M, Rahl F, Roldan LG (1969) J Polym Sci A-2: Polym Phys 7:463
91. Seeliger W, Aufderhaar E, Diepers W, Feinauer R, Nehring R, Thier W, Hellmann H (1966) Angew Chem Int Ed 5:875
92. Kujawa P, Aseyev V, Tenhu H, Winnik F (2006) Macromolecules 39:7686
93. Stock J, Burchard W, Stadler R (1992) Macromolecules 25:6885